International Journal of Biological Macromolecules 336 (2026) 149315

Contents lists available at ScienceDirect

International Journal of Biological Macromolecules

journal homepage: www.elsevier.com/locate/ijbiomac

In silico insights into the activation mechanism of the $P2Y_{12}$ receptor: Identification of a novel histidine-mediated microswitch

Francesco Fontanive [a], Alejandro Giorgetti [a,b,*]

[a] Department of Biotechnology, University of Verona, 37126, Italy
[b] IAS-5/INM-9 Jülich Forschungszentrum, Jülich, 52428, Germany

A B S T R A C T

The $P2Y_{12}$ receptor ($P2Y_{12}R$), a G protein–coupled receptor (GPCR) expressed predominantly on platelet membranes, is a key therapeutic target for the inhibition of platelet aggregation. Despite its clinical relevance, the molecular mechanism governing its activation remains incompletely understood. Here, we investigated the conformational dynamics underlying $P2Y_{12}R$ activation, focusing on the transition from the agonist-bound inactive state to the active conformation. Extensive all-atom molecular dynamics simulations were performed on $P2Y_{12}R$ complexed with the full agonist 2MeSADP. Essential dynamics analysis revealed that $P2Y_{12}R$ follows a conformational selection mechanism, whereby the receptor samples active-like conformations even in the absence of G-protein binding. This analysis also uncovered a previously uncharacterized microswitch acting as a critical driver of activation. To further dissect the molecular basis of receptor activation, we examined three canonical GPCR microswitches using multiple structural descriptors, elucidating their concerted roles in stabilizing intermediate and active states. The newly identified microswitch was subsequently used as a reaction coordinate in enhanced-sampling simulations, enabling reconstruction of the free energy landscape of the activation pathway. Together, these results provide a comprehensive molecular model of $P2Y_{12}R$ activation, advancing our understanding of GPCR activation and offering mechanistic insights that may guide the design of next-generation selective agonists and antagonists targeting this clinically important receptor.

1. Introduction

The $P2Y_{12}$ receptor ($P2Y_{12}R$), a G protein–coupled receptor (GPCR) and one of the eight members of the P2YR family expressed in humans [1–4], is prominently located on the cellular membrane of platelets and binds adenosine 5′-diphosphate (ADP), the first known low molecular weight platelet agonist [5]. Due to its location, the $P2Y_{12}R$ is involved in regulation of the physiological hemostasis process [6] and, therefore, it has become one of the most prominent clinical drug targets for inhibition of platelet aggregation. Currently, the antiaggregant drugs in use are Prasugrel, Clopidogrel, Ticagrelor and Cangrelor [7–10]. Despite the established efficacy of these pharmaceuticals in clinical practice, critical concerns persist, particularly regarding fatal bleeding events and variable effectiveness across patient populations [11–13]. The role of $P2Y_{12}R$ has also been investigated in inflammatory and neuropathic pain [14–16]. Uncovering the activation mechanism of $P2Y_{12}R$ is crucial. Thus, high-quality structural information is extremely important. Indeed, several solved structures in different activation states are present in the literature. In particular, two of them are of particular importance for this study: the crystal structure of $P2Y_{12}R$ bound to the full agonist 2MeSADP (PDB ID: 4PXZ), classified as an agonist-bound inactive state [17], and the crystal structure of $P2Y_{12}R$ bound to the full agonist 2MeSADP and the G-protein (PDB ID: 7XXI), representing the receptor in its fully active state [18]. Thanks to X-ray crystallography, these two distinct states of the receptor can be compared in a static manner, allowing for the identification of structural differences between them. The most notable differences include the conformation of helices V and VI: in the agonist-bound inactive state, helix V adopts a bent conformation, while helix VI is oriented inward toward the receptor's intracellular side. In contrast, the fully active state exhibits a straight conformation of helix V and an outward orientation of helix VI relative to the receptor's intracellular side. Based on this knowledge, the literature suggests structural features that differentiate the agonist-bound inactive and the fully active states. What remains unknown, however, is how the transition between these two states occurs. Biochemical and crystallographic methods combined with molecular dynamics simulations have provided models of the receptor activation driven by the action of "molecular switches" buried within the receptor structure [19,20]. Molecular switches can be defined as hotspots, i.e. key residues for biological activities [21] that are often functionally conserved across the entire class A GPCR [22,23]. More precisely, molecular switches involve subtle changes in distances and interactions between critical residues. This suggests that when an agonist binds to the orthosteric site, it induces minor rearrangement in the receptor's

* Corresponding author at: Department of Biotechnology, University of Verona, 37126, Italy.
E-mail addresses: francesco.fontanive@univr.it (F. Fontanive), alejandro.giorgetti@univr.it (A. Giorgetti).

https://doi.org/10.1016/j.ijbiomac.2025.149315
Received 30 July 2025; Received in revised form 19 November 2025; Accepted 26 November 2025
Available online 26 November 2025

residue packing, transmitting information from the binding site to other regions of the receptor, ultimately reaching the G-protein binding region [24,25]. As a result, specific critical residues act as "molecular switches", initiating residue repacking and conformational changes within the receptor. To investigate the molecular mechanism underlying the activation of the $P2Y_{12}R$ by the full agonist 2MeSADP, it is necessary to carry out an extensive sampling process. Here we have run MD simulations that allowed us to identify a novel molecular switch, that together with the canonical GPCR microswitches allow the exploration of active-like structures of the receptor even in the absence of the cognate G-protein. To elucidate the role of the novel microswitch, we run an enhanced sampling method, the Potential of Mean Force (PMF) with the accelerated weight histogram (AWH) method [26], in which the microswitch was considered as reaction coordinate. Our hypothesis is that the latter plays a pivotal role in the activation mechanism, contributing to the receptor's transition from the agonist-bound inactive state to the active state.

2. Results and discussion

2.1. Unbiased molecular dynamics simulation

A 1 μs unbiased molecular dynamics simulation was performed to investigate the structural and functional behavior of the $P2Y_{12}$ receptor under near-physiological conditions. The system consists of the $P2Y_{12}R$ embedded in a lipid bilayer composed of DOPC molecules, along with water molecules, sodium ions, and chloride ions (Table S1). The equilibration of the simulation was assessed by measuring the RMSD of the protein backbone after a least-squares fit to the protein backbone relative to the starting structure (Fig. S1). The RMSD values, ranging from 0.2 to 0.4 nm, suggest that the receptor undergoes moderate conformational changes over the course of the simulation. In fact, three distinct phases of RMSD fluctuation can be observed: the first phase (0–200 ns), the second phase (200–800 ns), and the third phase (800–1000 ns). The hypothesis is that these phases reflect conformational changes within the receptor, particularly when comparing the first and the third phases. The root mean square fluctuation (RMSF) was then calculated to identify regions of higher atomic mobility within the receptor. Several prominent peaks are visible in the plot (Fig. S2), indicating regions of higher atomic mobility (Fig. S3). As expected, these peaks correspond to flexible loops or terminal regions of the receptor. The most significant peaks are observed near residues in the N-terminus, ICL1, ICL2, ECL2, ICL3, and the terminus of helix VII. These observations suggest that the receptor maintains global stability while allowing for local flexibility, which could be relevant for its activation mechanism. We have performed three independent simulations of 1 μs each and calculated the RMSD for all replicates. The mean RMSD and its standard deviation across replicas are shown in Fig. S4.

2.2. Full agonist interactions in the binding site

RMSD's values of the binding pocket, including residues $LYS280^{7.34}$, $TYR259^{6.58}$, $ARG93^{3.21}$, $ARG256^{6.55}$, $GLN263^{6.62}$, $TYR105^{3.33}$, $HIS187^{5.36}$, $ASN191^{5.40}$, $ASN159^{4.60}$, $CYS97^{3.25}$, $LYS179^{ECL2}$, $VAL190^{5.39}$, $MET152^{4.53}$, $LEU155^{4.56}$ and $TYR109^{3.37}$, indicate that the binding site remains stable throughout the simulation, showing no significant structural deviations (Fig. S5). 2MeSADP's RMSD values along the entire simulation suggest that 2MeSADP is well-maintained in the binding pocket and does not exhibit significant deviations (Fig. S6). This behavior underscores the stability of the 2MeSADP-receptor interaction. Indeed, the full agonist binds to a site formed by helices III, IV, V, VI and VII [17]. In detail:

- The terminal unprotonated phosphate group of 2MeSADP interacts with residues of TM7, TM6 and TM3: $LYS280^{7.34}NH_3^+$ via an ionic bond, $TYR259^{6.58}OH$ via a hydrogen bond, and $ARG93^{3.21}$ via both ionic and hydrogen bonds (Fig. 1 and Fig. S7a).
- The unprotonated phosphate group bound to the ribose moiety forms stable interactions with residues of TM6, such as $ARG256^{6.55}$ via an ionic bond and $GLN263^{6.62}NH_2$ via a hydrogen bond. Additionally, it interacts with one residue of TM3, $TYR105^{3.33}OH$, through a stable hydrogen bond. Intriguingly, $TYR105^{3.33}$ also engages in a π-π interaction with the five-membered ring of the 2MeSADP adenine (Fig. 1 and Fig. S7b).
- The adenine moiety forms several interactions with residues of TM3, TM4 and TM5. The N7 of the adenine ring interacts with imidazole NHε group of $HIS187^{5.36}$ and the $ASN191^{5.40}NH_2$ via hydrogen bonds. The N3 of the adenine ring forms a hydrogen bond with $ASN159^{4.60}NH_2$, while the adenine amine group is hydrogen-bonded to $TYR109^{3.37}OH$ and the carboxamide C═O group of $ASN191^{5.40}$ (Fig. 1 and Fig. S7c).
- The ribose moiety of 2MeSADP interacts with residues of TM4, TM3, ECL2, and TM5. Specifically, $ASN159^{4.60}NH_2$ forms a hydrogen bond with the C3'-hydroxyl group, $CYS97^{3.25}C{=}O$ forms a hydrogen bond with the C2'-hydroxyl group, and $LYS179^{ECL2}NH_3^+$ forms ion-dipole interactions with both the C2'- and C3'-hydroxyl groups (Fig. 1 and Fig. S7d). $HIS187^{5.36}$ forms a hydrogen bond with C2'-hydroxyl group.
- The methyl-sulfur tail of 2MeSADP is enclosed within a hydrophobic pocket and interacts with residues of TM5, TM4, TM3, including $VAL190^{5.39}$, $MET152^{4.53}$, $LEU155^{4.56}$, and the phenyl group of $TYR109^{3.37}$, through hydrophobic interactions (Fig. 1 and Fig. S7e).

To assess the stability of the interactions listed above, we have calculated the frequency of formation of the interactions (Fig. S8) between 2MeSADP and the residues in the orthosteric binding site. Specifically, residues $TYR105^{3.33}$, $VAL102^{3.30}$, $HIS187^{5.36}$, $ASN191^{5.40}$, $LYS179^{ECL2}$, $VAL190^{5.39}$, $LYS280^{7.34}$, $ARG256^{6.55}$, $TYR109^{3.37}$, and $ARG93^{3.21}$ interact with the full agonist 2MeSADP for more than 60 % of the total simulation time.

2.3. Essential dynamics of the P2Y12R

The MD trajectory exhibits both local fluctuations and collective motions of $P2Y_{12}R$, making it challenging to identify functionally relevant movements of the receptor. We thus performed Principal Component Analysis [27] (PCA) of the trajectory to pinpoint the essential dynamics [28,29], i.e., the collective motions underlying the receptor's conformational changes. The first five eigenvectors account for 70 % of the total variance (Fig. S9). The projection of the first 5 eigenvectors as a function of time, along with their cosine contents, underscores that the trajectory has converged (Fig. S10). Interpolation between the extreme conformations sampled during the simulation along these eigenvectors enables pinpointing the Essential Dynamics of $P2Y_{12}R$. While Eigenvector 1 and 2 represent the broad movements of the flexible loops combined with helix motions, examination of the motion along the third eigenvector (8 % of the variance) reveals the movement of helix V from a bent to a vertical position, whereas the motion along the fifth eigenvector (5 % of the variance) illustrates a slight outward movement of helix VI. The motion along the fourth eigenvector (6 % of variance) shows the opposite movement expressed by eigenvector 3 and 5.

2.3.1. From PCA's conformational subspace to the Free energy landscape of $P2Y_{12}$

The PCA calculation, considering Principal Component 1 (PC1) and Principal Component 2 (PC2) allows the identification of the conformational subspace explored by the receptor during the entire MD simulation and thus were used to construct the conformational scatter plot. This is because PC1 and PC2 account for the largest fraction of the total variance (i.e., together over 50 %), thus providing a global overview of the conformational space sampled by the receptor. While PC3

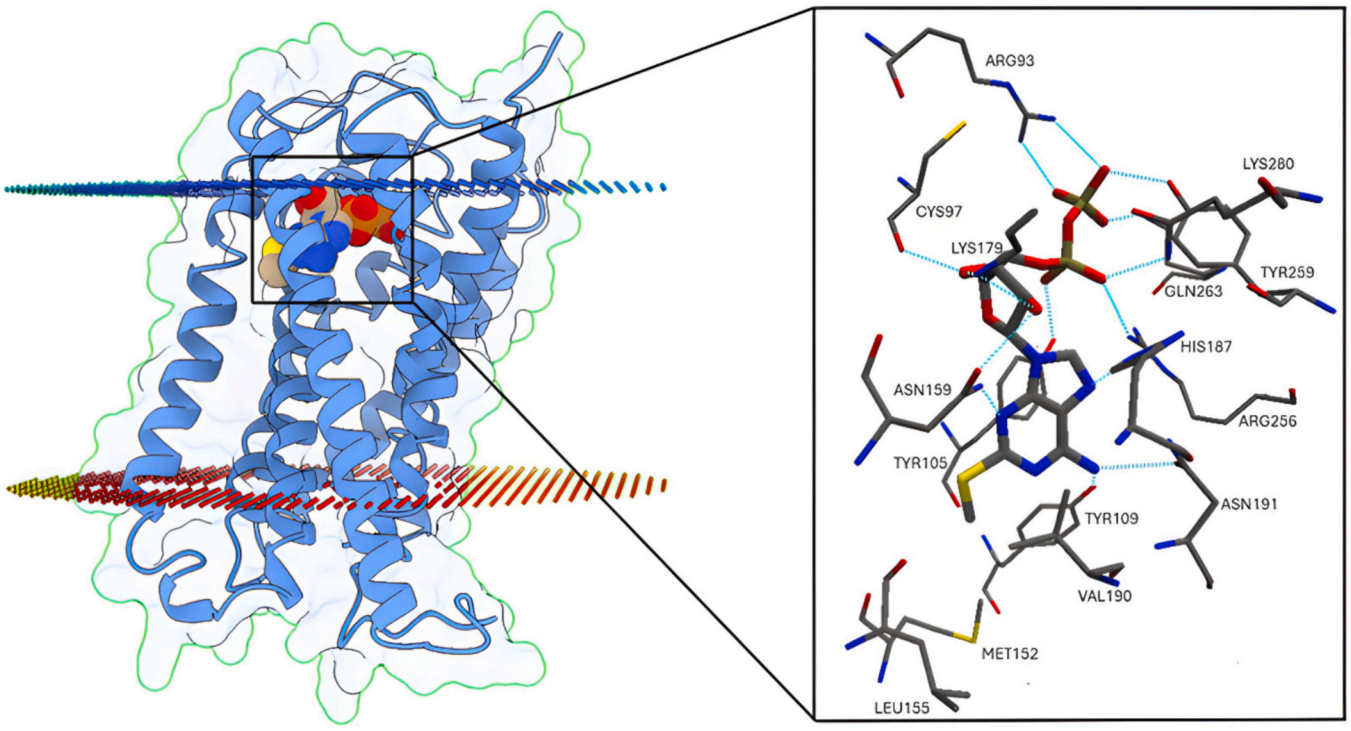

Fig. 1. *Structural representation of the P2Y$_{12}$ receptor bound to the full agonist 2MeSADP. Left: Overall view of the receptor (blue cartoon) embedded in a lipid bilayer (membrane boundaries shown as colored arrows) with the bound ligand 2MeSADP (space-filling model in red for oxygen, yellow for sulfur, blue for nitrogen, and grey for carbon). Right: Zoom-in of the orthosteric binding site showing key interactions between 2MeSADP and surrounding residues. Interactions (hydrogen bonds, ionic interactions and ion-dipole interactions) are indicated by cyan dashed lines.* (For interpretation of the references to color in this figure legend, the reader is referred to the web version of this article.)

and PC5 capture specific functional transitions (Fig. S11), PC1 and PC2 offer broader discrimination among major conformational states and energy minima, making them more suitable for visualizing the full landscape of sampled states and identifying statistically significant basins. In this context, PC1 and PC2 act as collective reaction coordinates for mapping the conformational ensemble, whereas PC3 and PC5 were used for functional interpretation of activation-related motions. From the conformational scatter plot, where each point corresponds to a specific receptor conformation (Fig. S12), we calculated the Gibbs free energy landscape. This is achieved by Boltzmann inverting multi-dimensional histograms, transforming the frequency distribution of conformational states (Fig. S13) into a quantitative Free energy surface. Indeed, the Free energy landscape (FEL) comprises 32 energy minima and features three main basins (Fig. 2).

We constructed sub-trajectories for the three energy minima and applied a clustering scheme [30]. We then superimposed the cluster representatives onto three experimental crystallographic structures, representing the two agonist-bound inactive states and the fully active state (Table 1 and Fig. 3). To provide a clearer structural interpretation of the binding differences observed, we visualized the 3D binding modes of the cluster representatives within the orthosteric pocket. The resulting models reveal subtle variations in ligand orientation and in the interaction network formed by key residues (Movie S1).

By combining the information extracted from the scatter plot (Fig. S12) and the FEL plot (Fig. 2), a dynamic view of the events occurring throughout the entire MD simulation is obtained (for details, see SI section: "Exploration of the conformational subspace: a dynamics view", and Fig. S14, Fig. S15, Fig. S16). Ultimately, PCA calculations have enabled the determination of the conformational subspace explored by the receptor during the simulation and has pinpointed the receptor's Essential Dynamics. In the context of Essential Dynamics, the helical movements within the P2Y$_{12}$R helical bundle are ultimately

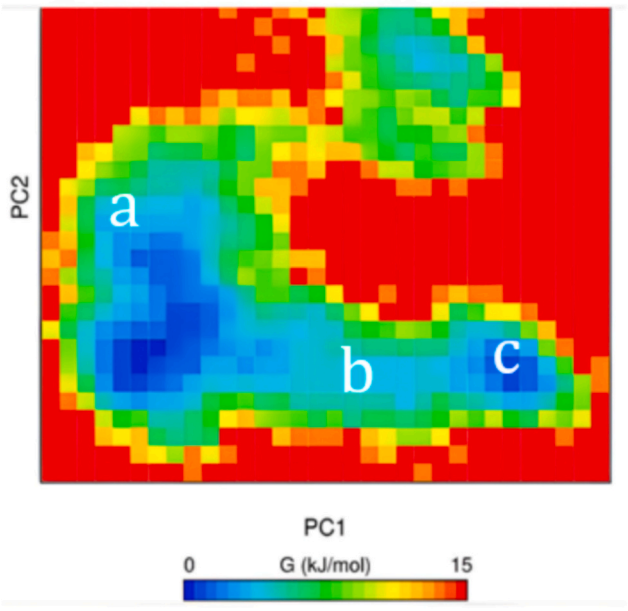

Fig. 2. *Free Energy Landscape, which comprises 32 energy minima and features three main basins. Letters a, b and c indicate the energy minima from which representative structures (#1, #2, #3) were extracted, as shown in* Table 1 *and* Fig. 3.

driven by the action of the so-called molecular switches.

2.4. TM3-TM6-TM7 angle displays the opening of the cytoplasmic cavity

To assess if the simulated system actually explores the active-like

Table 1
Conformations extracted from the FEL minima (a, b and c, as from Fig. 2) and compared with crystal structures of $P2Y_{12}R$.

Energy minimum	Cluster	Extraction time (ns)	Superimposed structure	RMSD (Å)
a, #1	8	161.200	$P2Y_{12}$-2MeSADP-G-protein	3.1
b, #2	2	798.750	$P2Y_{12}$-2MeSADP	3
c, #3	2	904.750	$P2Y_{12}$-2MeSATP	3.1

conformations of the receptor, we investigated the opening of the cytoplasmic cavity, by computing the distance between TM3 and TM6, as well as the angle defined by TM3–TM6–TM7. While the TM3–TM6 distance alone is not particularly informative, the TM3–TM6–TM7 angle exhibits a clear shift (Fig. S17) that reflects the opening of the cytoplasmic cavity. We also analyzed the distribution of the TM3–TM6–TM7 angle (Fig. S18). By combining the TM3–TM6 distance and the TM3–TM6–TM7 angle, we generated the corresponding Free energy surface (Fig. S19), which reveals two distinct minima located at 1.02 nm / 80° and 1.16 nm / 88°, respectively. The conformation extracted from minimum a,**#1** displays a TM3–TM6–TM7 angle of 88.5°, that from minimum b,**#2** shows an angle of 82.3°, and that from minimum c,**#3** exhibits an angle of 79.8°. The concurrent increase in both the TM3–TM6 distance and the TM3–TM6–TM7 angle indicates a concerted outward displacement of TM6, consistent with the opening of the cytoplasmic cavity.

2.5. Changes in the cytoplasmic cavity size

To complement the geometrical analysis, we quantified the evolution of the intracellular cavity volume of $P2Y_{12}R$. Indeed, to investigate the changes in the cytoplasmic cavity size, the evolution of the intracellular cavity volume of $P2Y_{12}R$ along the MD simulation was analyzed. For each trajectory frame, a three-dimensional grid with a 1 Å spacing was constructed around the geometric center defined by the Cα atoms of residues $R122^{3.50}$, $I212^{5.61}$, $R256^{6.55}$, and $Y298^{7.53}$, which delineate the intracellular entrance of the G-protein binding pocket. The orientation of helix TM6 was computed separately using the Cα atoms of residues 230–265 to obtain its principal axis and monitor its tilt throughout the simulation. Only grid points located in the cytoplasmic half of the receptor (–10 Å to +2 Å along the membrane normal) and within a 10 Å cylindrical region around the cavity axis were considered. Grid points within 3.9 Å of any protein atom were excluded, while those located within 2.0 Å of any water oxygen atom were classified as water accessible. The sum of these accessible voxels provided an estimate of the instantaneous cavity volume. Additionally, two structural descriptors of receptor activation were calculated: (i) the distance between the Cα atoms of $R122^{3.50}$ and $P230^{6.30}$, used as a proxy for TM6 displacement, and (ii) the tilt angle of TM6 relative to its orientation in the first frame. The resulting time series allowed us to correlate the enlargement of the intracellular cavity with the outward movement of TM6 and the formation of continuous water pathways toward the receptor core, as shown in Fig. S20. The time series revealed a progressive increase in the cavity size, from less than 100 $Å^3$ at the beginning of the simulation to over 1000 $Å^3$ in the final part of the trajectory. This expansion indicates a gradual opening of the intracellular cavity toward the cytoplasmic side, consistent with receptor activation and TM6 displacement.

2.6. Molecular switches

2.6.1. Canonical GPCR microswitches

It has been suggested [24] that an agonist bound to the orthosteric binding site induces subtle changes in the packing of receptor residues, transmitting information from the binding site to other regions of the receptor and eventually reaching the G-protein binding region. Indeed, agonist binding causes certain critical residues to function as "molecular switches", triggering residue repacking and conformational changes within the receptor. Hence, molecular switches underscore the dynamic nature of the receptor's conformational landscape, emphasizing their pivotal role in mediating its activation and function. We have thus investigated three canonical GPCR microswitches: the DRY motif, the PIF motif, and the NPxxY motif. The $P2Y_{12}$ receptor exhibits the following peculiarities: it lacks the $W^{6.48}$ residue that typically acts as a toggle switch, having an $F^{6.48}$ instead, and it also lacks the ionic lock between TM3 and TM6, as specified in ref. [31]. Moreover, in $P2Y_{12}R$, the hydrophobic PIF motif ($I^{3.40}$–$P^{5.50}$–$F^{6.44}$) highly conserved in class A

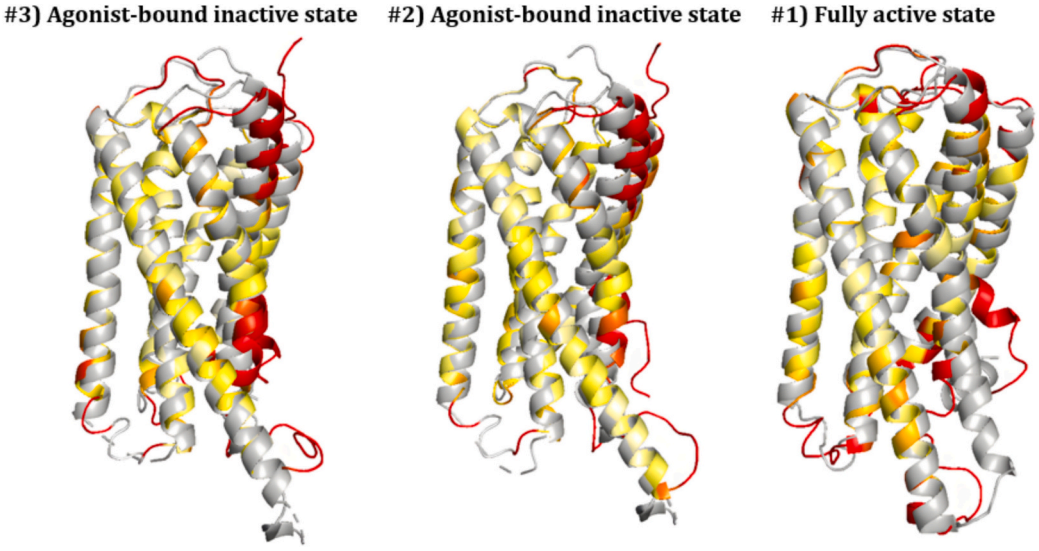

Fig. 3. *Relevant conformations from three different energy minima of the FEL.* ***#1)*** *Conformation extracted from minimum a superimposed with the crystal $P2Y_{12}$-2MeSADP-G-protein, representing the fully active state.* ***#2)*** *Conformation extracted from minimum b – superimposed with the crystal structure of $P2Y_{12}$-2MeSADP, representing an agonist-bound inactive state;* ***#3)*** *Conformation extracted from minimum c superimposed with the crystal structure of $P2Y_{12}$-2MeSATP, representing a partial agonist-bound inactive state. Extracted conformations are shown in color (white to red), while crystal structures are in grey. The color gradient reflects local RMSD values, highlighting structural deviations particularly in helices V and VI, which undergo significant rearrangements during activation.* (For interpretation of the references to color in this figure legend, the reader is referred to the web version of this article.)

GPCRs is replaced by NIV ($I^{3.40}$–$N^{5.50}$–$V^{6.44}$). This substitution, characterized by the presence of a polar residue at position 5.50, suggests a specific adaptation of $P2Y_{12}R$ to maintain the structural coupling between helices TM3, TM5, and TM6 in the absence of the conserved proline. This variant may influence the activation dynamics and the transmission of TM6 motion toward the cytoplasmic region. To investigate these three microswitches, we employed different structural metrics: the ΔRMSD for the NIV motif, the χ_1 dihedral angle of $Y^{7.53}$ for the NPxxY motif, and the radius of gyration of $R^{3.50}$ for the DRY motif. The rationale behind monitoring these metrics was to compare their behavior with respect to the crystal structures representing the fully active state (PDB ID: 7XXI) and the agonist-bound inactive state (PDB ID: 4PXZ). For the NIV motif, we focused on the dynamical behavior of residues $I^{3.40}$ and $V^{6.44}$ (as done by Dror et al. [32]), with the aim of comparing their dynamics during the simulation to those observed in the fully active (7XXI) and agonist-bound inactive (4PXZ) crystallographic structures. To this end, we calculated the RMSD of the residue pair with respect to each of the two crystal structures. We then computed the difference $\Delta RMSD = RMSD_{inactive} - RMSD_{active}$. The results are reported in Fig. S21. As shown in the upper part of the plot, the RMSD values with respect to the fully active and agonist-bound inactive states oscillate in a roughly mirrored manner, indicating transitions between active-like and inactive-like conformations. The lower part of the plot, which displays the ΔRMSD values, confirms this behavior and highlights whether the simulated conformations are closer to the active or inactive state: $\Delta RMSD < 0$ indicates conformations closer to the active state, whereas $\Delta RMSD > 0$ corresponds to conformations closer to the inactive state. The ΔRMSD time series remains predominantly slightly negative, indicating a mild bias toward active-like conformations, with transient positive excursions corresponding to brief visits to inactive-like states, particularly toward the end of the simulation. The distribution of ΔRMSD values for the $I112^{3.40}/V244^{6.44}$ pair is shown in Fig. S22. To further characterize the conformational space explored by the $I112^{3.40}/V244^{6.40}$ pair, we constructed a two-dimensional potential of mean force (PMF) as a function of the RMSD relative to the fully active (7XXI) and agonist-bound inactive (4PXZ) crystal structures (Fig. S23). The resulting Free energy surface reveals two main minima connected by a low-energy pathway, consistent with the coexistence of active-like and inactive-like conformations. The deepest minimum corresponds to conformations closer to the active state, in agreement with the ΔRMSD distribution and time series, which indicate a slight preference toward active-like conformations. The second, shallower minimum, located at higher RMSD values with respect to the agonist-bound inactive structure, represents transient excursions toward inactive-like conformations. These results suggest that the NIV motif undergoes subtle structural rearrangements, allowing reversible transitions between active-like and inactive-like states along the simulation. For the NPxxY motif, we focused on investigating the χ_1 dihedral angle of $Y^{7.53}$ with respect to the crystal structures representing the fully active state (PDB ID: 7XXI) and the agonist-bound inactive state. As shown in Fig. S24, the χ_1 angle fluctuates between two distinct regions, corresponding to the values observed in the fully active structure (7XXI, $\chi_1 \approx -50°$) and in the inactive reference (minimum b,#2, $\chi_1 \approx 90°$). The trajectory reveals multiple transitions between these two rotameric states, indicating that $Y298^{7.53}$ undergoes dynamic switching throughout the simulation. After an initial period in which χ_1 remains around 90°, corresponding to an inactive-like conformation, $TYR298^{7.53}$ adopts an active-like orientation for several nanoseconds before returning to the inactive-like state. Toward the end of the trajectory, the residue alternates more frequently between the two conformations. The distribution of the χ_1 dihedral angle for $TYR298^{7.53}$ is shown in Fig. S25. This dynamic equilibrium between rotameric states supports the role of the NPxxY motif as a key element in modulating the transition between active and inactive conformations in class A GPCRs. Finally, we focused on investigating the radius of gyration of $R122^{3.50}$ in the DRY motif with respect to the crystal structures representing the fully active state (7XXI) and the agonist-bound inactive state (4PXZ). The radius of gyration is a metric that indicates the compactness of a residue. As shown in Fig. S26, at the beginning of the simulation, $R122^{3.50}$ is highly compact and forms an ionic lock with residue $D121^{3.49}$. Subsequently, it adopts a radius of gyration much closer to that of the active state than to the agonist-bound inactive state, with a clear excursion toward the fully active conformation between 150 – 180 ns. The distribution of the radius of gyration for $R122^{3.50}$ is shown in Fig. S27. Overall, these results suggest that the DRY motif evolves toward an active-like configuration, even transiently sampling the fully active conformation. Taken together, the analyses of the NIV, NPxxY, and DRY motifs consistently reveal a partial shift of $P2Y_{12}R$ toward active-like conformations, highlighting the dynamic nature of its activation mechanism and the interplay between local rearrangements and global motions of TM helices.

2.6.2. P2Y12's molecular switches

To gain deeper insights into the activation mechanism of $P2Y_{12}R$, we looked for specific molecular determinants. Indeed, we have identified four different specific interactions that change upon the receptor's screening of FEL minima: Switch 1: $TYR105^{3.33}$ – $LYS280^{7.34}$; Switch 2: $ILE112^{3.40}$ – $ASN201^{5.50}$; Switch 3: $PHE198^{5.47}$ – $HIS253^{6.52}$; and Switch 4: $GLN195^{5.44}$ – $HIS253^{6.52}$ (Fig. 4, a-d).

In detail, residues involved in Switch 1 are located within the orthosteric binding site, specifically on helices III and VII, respectively. Accordingly, this molecular switch could be referred to as the "3-7 lock switch" [19,20]. The interaction is mediated by an ion-dipole interaction between $LYS280^{7.34}NH_3^+$ and $TYR105^{3.33}OH$, the latter being a functionally conserved residue across class A GPCR [22]. Switch 1 is defined by the disruption of this ion-dipole interaction, characterized by a sudden increase in their heavy atom distance, as shown in Fig. 4a. Residues forming Switches 2 and 3 are located between helices III, V, and VI. Residues of Switch 2 are situated in a region known as the "transmission switch" [19,20,23]. While residues in Switch 2 are connected by a hydrophobic contact between $ILE112^{3.40}$ and $ASN201^{5.50}$ that breaks during the simulation, as shown by a sharp increase in the Cα–Cα distance (Fig. 4b), Switch 3 involves a π–π stacking interaction between aromatic side chains. This specific molecular switch is identified by analyzing the improper dihedral angle between atoms $PHE198^{5.47}$:CE2, $PHE198^{5.47}$:CD1, $HIS253^{6.52}$:CD2, $HIS253^{6.52}$:CE1. This specific molecular switch could be identified as the "histidine toggle switch", a characteristic feature of the $P2Y_{12}$ receptor. A sudden "jump" in the dihedral angle is a clear marker of histidine rotamerization, as reported in Fig. 4c. Notably, $HIS253^{6.52}$ facilitates the identification of a fourth molecular switch (Switch 4), not yet fully characterized (Fig. 4d). Indeed, during histidine rotamerization, $HIS253^{6.52}$NHδ forms a hydrogen bond with the carboxyamide C═O group of $GLN195^{5.44}$. Consequently, the breaking and subsequent formation of this hydrogen bond defines molecular Switch 4. We speculate that a key role in the activation/deactivation of the receptor is mediated by the molecular switch between residues $HIS253^{6.52}$ and $GLN195^{5.44}$. $HIS253^{6.52}$ is located on helix VI, while $GLN195^{5.44}$ is located on helix V. Our hypothesis is that this specific molecular switch plays a pivotal role in facilitating the transition of helix V from a bent to a vertical position and the outward displacement of helix VI. The peculiarity of this molecular switch lies in the rotamerization of histidine and the subsequent formation of a hydrogen bond between the NHδ of $HIS253^{6.52}$ and the carboxyamide C═O group of $GLN195^{5.44}$. Moreover, the receptor conformation superimposed onto the P2Y12-2MeSADP crystal structure reveals two additional hydrogen bonds: one between the terminal NH_2 of the $GLN195^{5.44}$ side chain and the carbonyl C═O group of $HIS253^{6.52}$, and another between the carboxyamide C═O group of $GLN195^{5.44}$ and the protonated nitrogen atom of $TRP199^{5.48}$ (Fig. S28). These additional hydrogen bonds are also present in the receptor conformation superimposed onto the P2Y12-2MeSATP. Our hypothesis is that this cluster of hydrogen bonds acts as a lock, restricting the movement of helices V and VI and defining these two conformations as the agonist-bound inactive

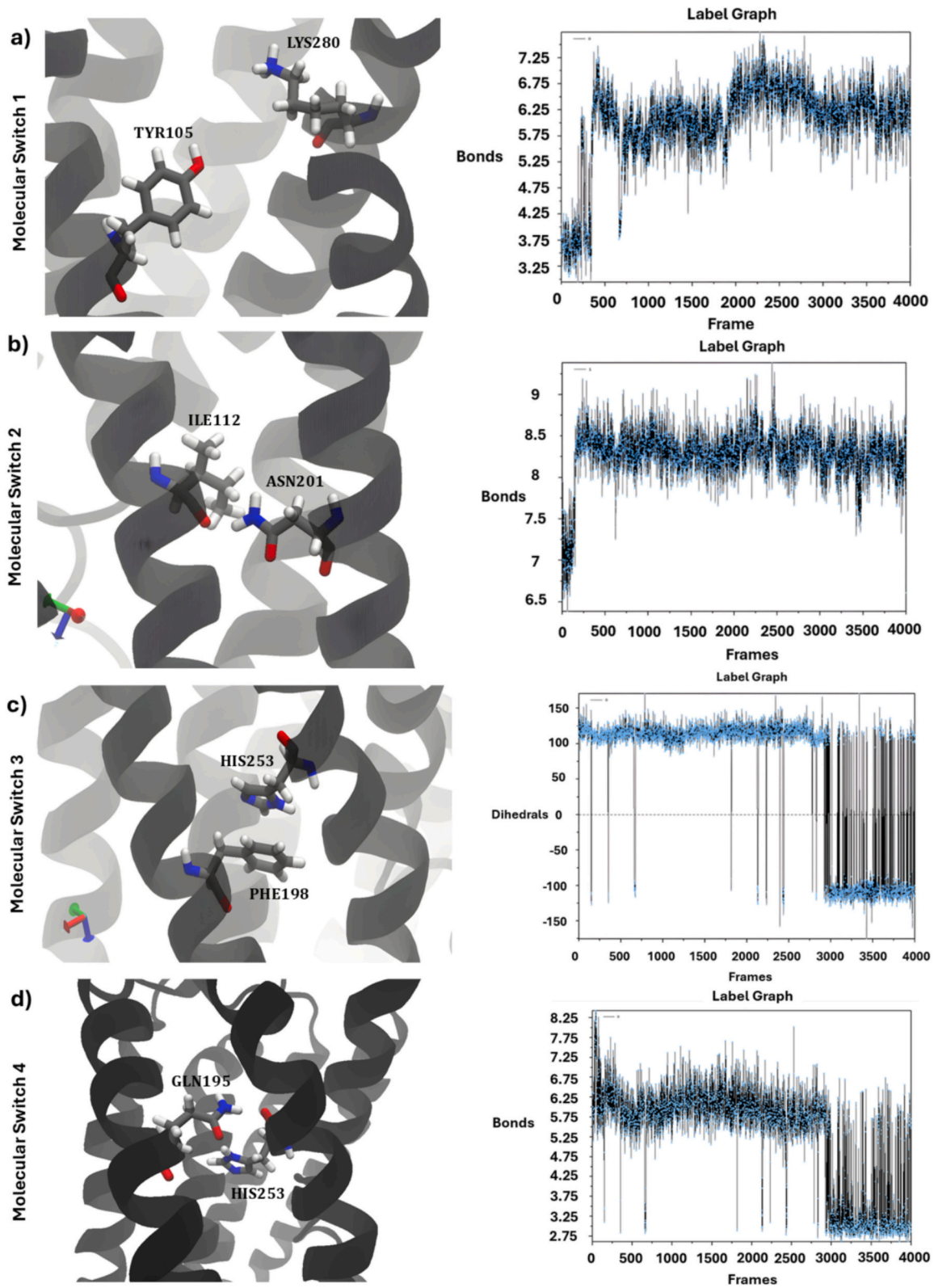

Fig. 4. a) *Molecular Switch 1: TYR105 – LYS280. Ion-dipole interaction between LYS280$^{7.34}NH_3^+$ and TYR105$^{3.33}$OH; the disruption of this interaction is marked by a sudden increase in the heavy atoms distance, defining the switch behavior;* b) *Molecular Switch 2: ILE112 – ASN201. ILE112$^{3.40}$ – ASN201$^{5.50}$ interact* via *hydrophobic contacts and a sharp increase in the Cα - Cα distances between the two residues explains its function;* c) *Molecular Switch 3: PHE198 – HIS253. PHE198$^{5.47}$ – HIS253$^{6.52}$ could be identified as the "histidine toggle switch" where a sudden "jump" in the dihedral angle is a clear marker of histidine rotamerization;* d) *Molecular Switch 4: GLN195 – HIS253. During histidine rotamerization, HIS253$^{6.52}$NHδ forms a hydrogen bond with the carboxyamide C═O group of GLN195$^{5.44}$; the breaking and subsequent formation of this hydrogen bond defines this molecular switch.*

state. Conversely, the receptor conformation superimposed onto the $P2Y_{12}$-2MeSADP-G-protein crystal structure retains the latter two hydrogen bonds, while the hydrogen bond between the NHδ of $HIS253^{6.52}$ and the carboxyamide C═O group of $GLN195^{5.44}$ is not formed (Fig. S29).

2.7. PMF

These findings collectively highlight the critical role of molecular switches in orchestrating receptor activation, emphasizing the intricate interplay between structural transitions and functional states. To further investigate the specific Switch 4, i.e., the rotamerization of histidine and the subsequent formation of the hydrogen bond between the NHδ of $HIS253^{6.52}$ and the carboxyamide C═O group of $GLN195^{5.44}$, we employed the Potential of Mean Forces (PMF) with accelerated weight histogram (AWH) method [26]. This approach enabled the setting up of a new simulation of the system, allowing us to scan this reaction coordinate and study the underlying process in detail. Switch 4 was chosen as the collective variable for enhanced sampling due to its central position within the receptor's transmembrane core, its direct structural involvement in the movement of helices V and VI, and its dynamic behavior observed during the unbiased simulation. The rotamerization of $HIS253^{6.52}$ appears to trigger a rearrangement of inter-helical hydrogen bonds that correlates with the transition toward the active state, making it a suitable and mechanistically relevant target for PMF analysis. PMF provides insights into the energy minimum and the activation barrier of the reaction. The accelerated weight histogram (AWH) method is an extended ensemble sampling technique which adaptively biases the simulation to promote exploration of the Free energy landscape [26,33], enabling the capture of rare events that typically occur on the millisecond timescale [34,35]. The aim was to scan a reaction coordinate to gain insight into the energy minimum and the heights of the energy barriers. After the simulation, key convergence metrics were assessed: five covering times were recorded at $t = 332.8$ ps, 1212.8 ps, 5238.4 ps, 14,812.8 ps and 21,161.6 ps; the simulation exited the initial bias estimation phase at $t = 21{,}161.6$ ps, completing a few transitions thereafter (Fig. S30); to assess the reliability of the bias estimate, the probability distribution of the reaction coordinate was compared with the reference distribution to ensure that the applied force constant (192,000 kJ/(mol*nmˆ2)) was appropriate (Fig. S31); additionally, the agreement between the sampled and target distributions confirms that the system has properly explored the free energy landscape, ensuring that the biasing force was well-calibrated and that no additional sampling is required (Fig. S32). The Potential of Mean Force for the scanned hydrogen bond characterizing Switch 4 exhibits three energy minima and two reaction barriers (Fig. 5).

The higher barrier has an energy of approximately 6.8 k_bT, equivalent to ~17 kJ/mol, while the lower barrier has an energy of approximately 3 k_bT, equivalent to ~7.5 kJ/mol. These energy barriers are consistent with the typical hydrogen-bond strengths reported for proteins embedded in membrane or other low-dielectric environments, where hydrogen bonds are moderately stronger than in water but weaker than in vacuum [36]. These results indicate that the formation and breaking of this hydrogen bond are energetically feasible and may lead to a release of constraints on helices V and VI. This process could explain the helical movements from a molecular perspective, facilitating the formation of the crevice required for G-protein accommodation. During the simulation, while scanning Switch 4, three dynamic events occur, as described in Table 2.

Notably, the crystal structure of $P2Y_{12}$-2MeSADP-G-protein also adopts the same conformation for residue $GLN195^{5.44}$, while $HIS253^{6.52}$ has not undergone rotamerization. Based on the above-mentioned events observed during the simulation, three receptor conformations were extracted from the trajectory based on the distance between the NHδ of $HIS253^{6.52}$ and the carboxyamide C═O group of $GLN195^{5.44}$ that reflects the minima of Fig. 5, as reported in Table 3 and Fig. 6.

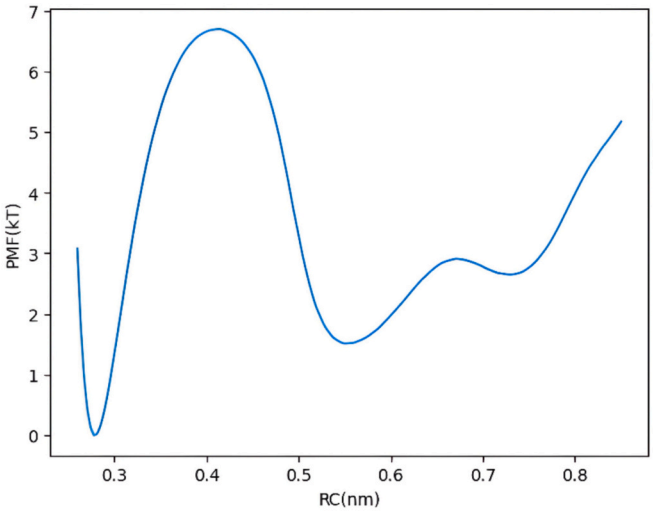

Fig. 5. *The Potential of Mean Force for the scanned hydrogen bond characterizing Switch 4 exhibits three energy minima and two reaction barriers.*

Table 2
Summary of dynamic events observed during the 500 ns simulation, describing the conformational changes of $GLN195^{5.44}$ and its interactions with $HIS253^{6.52}$ and $TRP199^{5.48}$.

Time interval (ns)	Event description
87–206	The side chain of GLN195 orients away from HIS253 toward 2MeSADP
207–391	The terminal NH_2 of GLN195 forms a hydrogen bond with the carbonyl C═O group of HIS253. The carboxyamide C═O group of GLN195 forms another hydrogen bond with the protonated nitrogen atom of TRP199
392–500	The GLN195 side chain undergoes a flip-flop movement. The terminal NH_2 is positioned above the protonated nitrogen atom of TRP199 and forms a hydrogen bond with the carbonyl group of HIS253. The carboxyamide C═O group of GLN195 forms a hydrogen bond with the NHδ of HIS253, which undergoes a distinct rotamerization

The superposition of conformation #3 with the crystal structure of the fully active $P2Y_{12}$-2MeSADP-G-protein (Fig. 6) exhibits an RMSD value of 3 Å relative to the crystal structure, indicating that the simulation along the reaction coordinate was able to capture the role of Switch 4 in the activation mechanism of the receptor.

Indeed, these findings support our hypothesis: the breaking and formation of the hydrogen bond between the NHδ of $HIS253^{6.52}$ and the carboxyamide C═O group of $GLN195^{5.44}$ is not only reproducible but also plays a pivotal role in regulating the activation/deactivation mechanism of $P2Y_{12}R$. Although the biased molecular dynamics simulation does not fully achieve the histidine conformation observed in the $P2Y_{12}$-2MeSADP-G-protein crystal structure, we speculate that the presence of the G-protein facilitates histidine rotamerization, thereby driving the receptor toward its active conformation.

Table 3
Receptor conformation extracted from the trajectory based on the distance between the NHδ of $HIS253^{6.52}$ and the carboxyamide C═O group of $GLN195^{5.44}$.

Conformation	Extraction time (ns)	Hydrogen bond length (Å)
#1	194	5.5
#2	335	7.4
#3	465	2.8

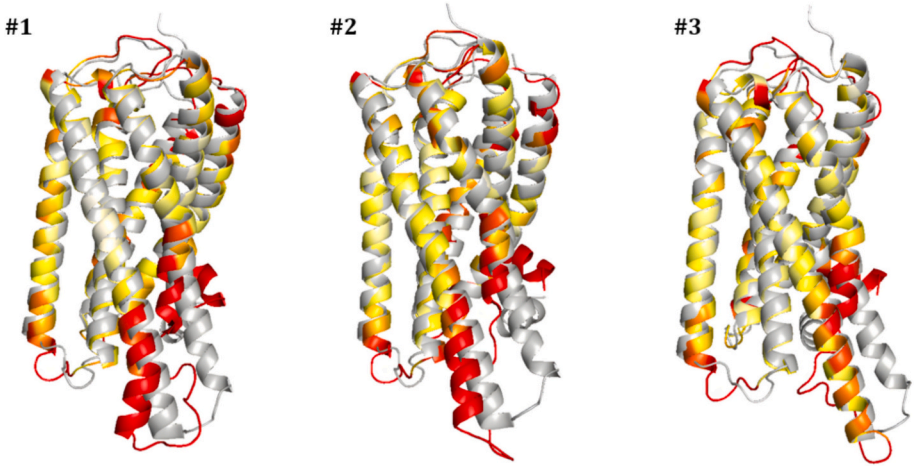

Fig. 6. *Receptor conformations extracted from the biased molecular dynamics simulation. #***1)** *Conformation extracted at 194 ns superimposed with the crystal structure $P2Y_{12}$-2MeSADP-G-protein; #***2)** *conformation extracted at 334 ns superimposed with the crystal structure $P2Y_{12}$-2MeSADP-G-protein; #***3)** *conformation extracted at 465 ns superimposed with the crystal structure $P2Y_{12}$-2MeSADP-G-protein. The figure highlights conformational changes in helices V and VI. Superposition of conformation 3 with the crystal structure of fully active $P2Y_{12}$-2MeSADP-G-protein indicates that the simulation along the reaction coordinate successfully captured the role of Switch 4 in the receptor's activation mechanism. Extracted conformations are shown in color (white to red), while the crystal structure in grey. The color gradient reflects local RMSD values, highlighting structural deviations – particularly in helices V and VI, which undergo major rearrangements during activation.* (For interpretation of the references to color in this figure legend, the reader is referred to the web version of this article.)

3. Conclusions

In this study, we investigated the activation mechanism of $P2Y_{12}R$. Extensive MD simulations were conducted with the receptor bound to the full agonist 2MeSADP, starting from its experimental structure that represents an agonist-bound inactive state. After the simulation, we first analyzed the interactions between the full agonist and the residues in the orthosteric binding site, finding good agreement with those reported in the literature [17]. We then used Principal Component Analysis to identify the receptor's Essential Dynamics, revealing key helical movements involved in the activation process. Using the insights gained from PCA, we then constructed the Free energy landscape. By extracting conformations from three energy minima of the FEL, we superimposed them onto crystal structures representing the agonist-bound inactive states, the partial agonist-bound inactive state, and the active state. To explain helical movements from a molecular perspective, the MD trajectory was analyzed to investigate the canonical GPCR microswitches and to identify specific molecular switches, revealing four types that indicate changes within the receptor. Specifically, a hydrogen bond was identified as a reaction coordinate and was scanned using an enhanced sampling method, providing insights into energy barriers and energetic minima. The findings of the PMF simulation suggest that the breaking and formation of this hydrogen bond facilitates the release of constraints on helices V and VI, enabling the receptor to transition into the active conformation. The PMF investigation focused on an in silico study of the molecular mechanism underlying the transition from the agonist-bound inactive state to an active-like state. On the other hand, the unbiased MD simulation supports the conformational selection theory, as active-like conformations were sampled even in the absence of the G protein; further experimental investigations could help validate our computational findings. Although full activation of GPCRs typically requires the presence of the G-protein and occurs on longer timescales, our 1 μs simulation revealed transient sampling of conformations closely matching the crystallographic active state. This observation suggests that agonist binding stabilizes pre-existing active-like conformations within the receptor's conformational ensemble, consistent with the conformational selection model. Together, these results provide a comprehensive molecular model of $P2Y_{12}R$ activation, advancing our understanding of GPCR activation and offering mechanistic insights that may guide the design of next-generation selective agonists and antagonists targeting this clinically important receptor.

4. Materials and methods

4.1. System preparation and MD simulations

The starting structure for the MD simulation was the crystal structure of P2Y12 receptor in complex with the full agonist 2MeSADP (PDB ID: 4PXZ) [17]. A homology modelling of the missing loop structures with the Swiss-Model program [37,38] using default parameters was performed. The receptor was embedded in a membrane of DOPC molecules using CHARMM-GUI webserver [39,40]. The system was inserted in a simulation box of size 8 nm × 8 nm × 9.4 nm. With this choice, the minimum distance between periodic images of the protein was larger than 2 nm. Water, sodium and chloride ions were added in order to solvate and neutralize the system at an ionic strength of 0.15 M. The final system comprised 61,661 atoms. The Amber99SB force field [41], the Slipids [42,43] and the TIP3P [44] force fields were used for the protein and ions, the lipids, and the water molecules, respectively. The General Amber Force Field (GAFF) parameters [45] were used for the ligand 2MeSADP, along with the AM1-BCC atomic charge [46]. 2MeSADP parametrization was performed with Antechamber software tool [47], whereas the Antechamber Python parser interface [48] was used to obtain suitable files for Gromacs. MD simulations were performed using Gromacs v2019.6 package [49,50]. The Particle Mesh Ewald method [51] was used to treat the long-range electrostatic interaction with a real space cutoff of 1.2 nm. A 1.2-nm cutoff was used for the short-range non-bonded interaction. A time step of 2 fs was set. The LINCS algorithm [52] was applied to constrain all bonds involving hydrogen atoms. The system underwent energy minimization using the steepest descent algorithm, followed by a NVT equilibration of 100 ps under periodic boundary conditions with positional restraints using a force constant of 1000 kJ/mol nm^{-2} on all the heavy atoms of the protein. Constant temperature condition was achieved via two independent coupling groups, namely, protein, 2MeSADP, DOPC, and water and ions, to velocity-rescaling thermostat [53] at 300 K. The same set up was used for the NPT equilibration of 1 ns, with the difference that the constant temperature and pressure conditions were achieved via the two independently coupling groups to Nosé-Hoover thermostat [54] at 300 K and Parrinello-Rahman barostat [55] at 1 bar. 1 μs MD was performed

removing all the restraints, with coordinates, velocities and energies collected every 50 ps. The following operations were performed for the cluster analysis: Principal Component analysis (PCA) was conducted on the raw trajectory, and the Free energy landscape (FEL) was plotted. Frames corresponding to each energy minimum of the FEL were collected, and sub-trajectories were constructed. A clustering algorithm – the Gromos method [30] – was applied to each sub-trajectory to obtain representative clusters of receptor conformations. Gromos clustering was performed using a cutoff of 0.1 nm. This workflow ensures that the representative clusters capture the key conformational states of the receptor within each energy minimum of the FEL. For comparison of activation metrics, the χ_1 dihedral angle of residue $Y298^{7.53}$ (NPxxY motif) was analyzed with respect to the fully active crystal structure (PDB ID: 7XXI) and the agonist-bound inactive-state reference (PDB ID: 4PXZ). Since $Y298^{7.53}$ in the 4PXZ crystal structure lacks side-chain atoms, the conformation corresponding to FEL minimum b,#2 from the simulation was used as the inactive-state reference for χ_1 dihedral angle calculations. The potential of mean force for scanning the hydrogen bond between the NHδ of $HIS253^{6.52}$ and the carboxyamide C=O group of $GLN195^{5.44}$ was calculated using the accelerated weight histogram (AWH) method [26], following the protocol outlined in the GROMACS manual (https://tutorials.gromacs.org/docs/awh-tutorial.html). The relevant parameters added to the .mdp file are listed in the Supplementary Materials. The simulation was run for 500 ns using a single walker.

CRediT authorship contribution statement

Francesco Fontanive: Writing – review & editing, Writing – original draft, Visualization, Investigation, Formal analysis, Data curation, Conceptualization. **Alejandro Giorgetti:** Writing – review & editing, Supervision, Resources, Methodology, Funding acquisition, Conceptualization.

Declaration of competing interest

The authors declare that they have no known competing financial interests or personal relationships that could have appeared to influence the work reported in this paper.

Appendix A. Supplementary data

Supplementary data to this article can be found online at https://doi.org/10.1016/j.ijbiomac.2025.149315.

Data availability

Data will be made available on request.

References

[1] M.P. Abbracchio, G. Burnstock, J.M. Boeynaems, et al., International Union of Pharmacology LVIII: update on the P2Y G protein-coupled nucleotide receptors: from molecular mechanisms and pathophysiology to therapy, Pharmacol. Rev. 58 (2006) 281–341, https://doi.org/10.1124/pr.58.3.3.

[2] I. von Kügelgen, Pharmacological characterization of P2Y receptor subtypes– an update, Purinergic Signal 20 (2) (2024) 99–108, https://doi.org/10.1007/s11302-023-09963-w.

[3] B. Hechler, C. Gachet, Purinergic receptors in thrombosis and inflammation, Arterioscler. Thromb. Vasc. Biol. 35 (11) (2015) 2307–2315, https://doi.org/10.1161/ATVBAHA.115.303395.

[4] K.A. Jacobson, C.E. Müller, Medicinal chemistry of adenosine, P2Y and P2X receptors, Neuropharmacology 104 (2016) 31–49, https://doi.org/10.1016/j.neuropharm.2015.12.001.

[5] M. Cattaneo, P2Y12 receptors: structure and function, J. Thromb. Haemost. 13 (2015) S10–S16, https://doi.org/10.1111/jth.12952.

[6] I.A. Jagroop, G. Burnstock, D.P. Mikhailidis, Both the ADP receptors P2Y1 and P2Y12, play a role in controlling shape change in human platelets, Platelets 14 (2003) 15–20, https://doi.org/10.1080/0953710021000062914.

[7] A. Majithia, D.L. Bhatt, Novel antiplatelet therapies for Atherothrombotic diseases, Arterioscler. Thromb. Vasc. Biol. 39 (2019) 546–557, https://doi.org/10.1161/ATVBAHA.118.310955.

[8] C. Patrono, J. Morais, C. Baigent, et al., Antiplatelet agents for the treatment and prevention of coronary Atherothrombosis, J. Am. Coll. Cardiol. 3 (70) (2017) 1760–1776, https://doi.org/10.1016/j.jacc.2017.08.037.

[9] D. Capodanno, D.J. Angiolillo, Timing, selection, modulation, and duration of $P2Y_{12}$ inhibitors for patients with acute coronary syndromes undergoing PCI, JACC Cardiovasc. Interv. 16 (1) (2023) 1–18, https://doi.org/10.1016/j.jcin.2022.10.023.

[10] D.J. Angiolillo, M. Galli, D. Alexopoulos, et al., International consensus statement on platelet function and genetic testing in percutaneous coronary intervention: 2024 update, JACC Cardiovasc. Interv. 17 (22) (2024) 2639–2663, https://doi.org/10.1016/j.jcin.2024.08.027.

[11] A. Briasoulis, T. Telila, M. Palla, et al., P2Y12 receptor antagonists: which one to choose? A systematic review and Meta-analysis, Curr. Pharm. Des. 22 (2016) 4568–4576, https://doi.org/10.2174/1381612822666160608114424.

[12] J.E. Yun, Y.J. Kim, J.J. Park, et al., Safety and effectiveness of contemporary P2Y12 inhibitors in an east Asian population with acute coronary syndrome: a Nationwide population-based cohort study, J. Am. Heart Assoc. 16 (8) (2019) e012078, https://doi.org/10.1161/JAHA.119.01207.

[13] G. Passacquale G, P. Sharma, D. Perera, A. Ferro, Antiplatelet therapy in cardiovascular disease: current status and future directions, Br. J. Clin. Pharmacol. 88 (6) (2022) 2686–2699, https://doi.org/10.1111/bcp.15221.

[14] G. Horváth, F. Gölöncsér, C. Csölle, et al., Central P2Y12 receptor blockade alleviates inflammatory and neuropathic pain and cytokine production in rodents, Neurobiol. Dis. 70 (2014) 162–178, https://doi.org/10.1016/j.nbd.2014.06.011.

[15] W.A.E. Parker, R.F. Storey, The role of platelet $P2Y_{12}$ receptors in inflammation, Br. J. Pharmacol. 181 (4) (2024) 515–531, https://doi.org/10.1111/bph.16256.

[16] P. Illes P, G.Y. Xu, Y. Tang, Purinergic signaling in the central nervous system in health and disease, Neurosci. Bull. 36 (11) (2020) 1239–1241, https://doi.org/10.1007/s12264-020-00602-7.

[17] J. Zhang, K. Zhang, Z.G. Gao, et al., Agonist-bound structure of the human P2Y12 receptor, Nature 1 (509) (2014) 119–122, https://doi.org/10.1038/nature13288.

[18] B. Li, S. Han, M. Wang, et al., Structural insights into signal transduction of the purinergic receptors P2Y1R and P2Y12R, Protein Cell 8 (14) (2023) 382–386, https://doi.org/10.1093/procel/pwac025.

[19] B. Trzaskowski, D. Latek, S. Yuan, et al., Action of molecular switches in GPCRs–theoretical and experimental studies, Curr. Med. Chem. 19 (2012) 1090–1109, https://doi.org/10.2174/092986712799320556.

[20] S. Filipek, Molecular switches in GPCRs, Curr. Opin. Struct. Biol. 55 (2019) 114–120, https://doi.org/10.1016/j.sbi.2019.03.017.

[21] F. Baldessari, R. Capelli, P. Carloni, A. Giorgetti, Coevolutionary data-based interaction networks approach highlighting key residues across protein families: the case of the G-protein coupled receptors, Comput. Struct, Biotechnol. J. 18 (2020) 1153–1159, https://doi.org/10.1016/j.csbj.2020.05.003.

[22] E. Suku, A. Giorgetti, Common evolutionary binding mode of rhodopsin-like GPCRs: Insights from structural bioinformatics, in: AIMS. Biophysics 4, AIMS Press, 2017, pp. 543–556, https://doi.org/10.3934/biophy.2017.4.543.

[23] Q. Zhou, D. Yang, M. Wu, et al., Common activation mechanism of class a GPCRs, Elife 8 (2019) e50279, https://doi.org/10.7554/eLife.50279.

[24] A.J. Venkatakrishnan, X. Deupi, G. Lebon, et al., Diverse activation pathways in class a GPCRs converge near the G-protein-coupling region, Nature 536 (7617) (2016) 484–487, https://doi.org/10.1038/nature19107.

[25] W.I. Weis, B.K. Kobilka, The molecular basis of G protein-coupled receptor activation, Annu. Rev. Biochem. 87 (2018) 897–919, https://doi.org/10.1146/annurev-biochem-060614-033910.

[26] V. Lindahl, J. Lidmar, B. Hess, Accelerated weight histogram method for exploring free energy landscapes, J. Chem. Phys. 141 (4) (2014) 044110, https://doi.org/10.1063/1.4890371.

[27] 26. 19 C.C. David, D.J. Jacobs, Principal component analysis: A method for determining the essential dynamics of proteins, in: D. Livesay (Ed.), Protein Dynamics. Methods in Molecular Biology 1084, Humana Press, Totowa, NJ, 2014, pp. 193–226, https://doi.org/10.1007/978-1-62703-658-0_11.

[28] 27. 20 H.J. Berendsen, S. Hayward, Collective protein dynamics in relation to function, Curr. Opin. Struct. Biol. 10 (2) (2000) 165–169, https://doi.org/10.1016/S0959-440X(00)00061-0.

[29] 28. 21 A. Amadei, A.B. Linssen, H.J. Berendsen, Essential dynamics of proteins, Proteins 17 (4) (1993) 412–425, https://doi.org/10.1002/prot.340170408.

[30] X. Daura, W.F. van Gunsteren, B. Jaun, Peptide folding: when simulation meets experiment, Angew. Chem. Int. Ed. 38 (1999) 236–240, https://doi.org/10.1002/(SICI)1521-3773(19990115)38:1/2<236::AID-ANIE236>3.0.CO;2-M.

[31] K. Zhang, J. Zhang, Z.G. Gao, et al., Structure of the human P2Y12 receptor in complex with an antithrombotic drug, Nature 1 (509) (2014) 115–118, https://doi.org/10.1038/nature13083.

[32] R.O. Dror, D.H. Arlow, P. Maragakis, et al., Activation mechanism of the β2-adrenergic receptor, Proc. Natl. Acad. Sci. USA 15;108(46) (2011) 18684–18689, https://doi.org/10.1073/pnas.1110499108.

[33] V. Lindahl, P. Gourdon, M. Andersson, B. Hess, Permeability and ammonia selectivity in aquaporin TIP2;1: linking structure to function, Sci. Rep. 8 (2018) 2995, https://doi.org/10.1038/s41598-018-21357-2.

[34] V. Lindahl, A. Villa, B. Hess, Sequence dependency of canonical base pair opening in the DNA double helix, PLoS Comput. Biol. 13 (4) (2017) e1005463, https://doi.org/10.1371/journal.pcbi.1005463.

[35] D. Coman, I.M. Russu, A nuclear magnetic resonance investigation of the energetics of basepair opening pathways in DNA, Biophys. J. 89 (5) (2005) 3285–3292, https://doi.org/10.1529/biophysj.105.065763.
[36] S.Y. Sheu, E.W. Schlag, H.L. Selzle, et al., Hydrogen bonds in membrane proteins, J. Phys. Chem. B 113 (15) (2009) 5318–5326.
[37] T. Schwede, J. Kopp, N. Guex, M.C. Peitsch, SWISS-MODEL: an automated protein homology-modeling server, Nucleic Acids Res. 31 (13) (2003) 3381–3385, https://doi.org/10.1093/nar/gkg520.
[38] A. Waterhouse, M. Bertoni, S. Bienert, et al., SWISS-MODEL: homology modelling of protein structures and complexes, Nucleic Acids Res. 46 (W1) (2018) W296–W303, https://doi.org/10.1093/nar/gky427.
[39] S. Jo, T. Kim, V.G. Iyer, W. Im, CHARMM-GUI: a web-based graphical user interface for CHARMM, J. Comput. Chem. 29 (11) (2008) 1859–1865, https://doi.org/10.1002/jcc.20945.
[40] J. Lee, X. Cheng, J.M. Swails, et al., CHARMM-GUI input generator for NAMD, GROMACS, AMBER, OpenMM, and CHARMM/OpenMM simulations using the CHARMM36 additive force field, J. Chem. Theory Comput. 12 (1) (2016) 405–413, https://doi.org/10.1021/acs.jctc.5b00935.
[41] V. Hornak, R. Abel, A. Okur, et al., Comparison of multiple Amber force fields and development of improved protein backbone parameters, Proteins 65 (3) (2006) 712–725, https://doi.org/10.1002/prot.21123.
[42] J.P. Jämbeck, A.P. Lyubartsev, Derivation and systematic validation of a refined all-atom force field for phosphatidylcholine lipids, J. Phys. Chem. B 116 (10) (2012) 3164–3179, https://doi.org/10.1021/jp212503e.
[43] J.P. Jämbeck, A.P. Lyubartsev, An extension and further validation of an all-atomistic force field for biological membranes, J. Chem. Theory Comput. 8 (8) (2012) 2938–2948, https://doi.org/10.1021/ct300342n.
[44] W.L. Jorgensen, J. Chandrasekhar, J.D. Madura, et al., Comparison of simple potential functions for simulating liquid water, J. Chem. Phys. 79 (1983) 926–935, https://doi.org/10.1063/1.445869.
[45] J. Wang, R.M. Wolf, J.W. Caldwell, et al., Development and testing of a general amber force field, J. Comput. Chem. 25 (9) (2004) 1157–1174, https://doi.org/10.1002/jcc.20035.
[46] A. Jakalian, D.B. Jack, C.I. Bayly, Fast, efficient generation of high-quality atomic charges. AM1-BCC model: II. Parameterization and validation, J. Comput. Chem. 23 (16) (2002) 1623–1641, https://doi.org/10.1002/jcc.10128.
[47] J. Wang, W. Wang, P.A. Kollman, D.A. Case, Antechamber: An Accessory Software Package for Molecular Mechanical Calculations, J. Chem. Inf, Comp, 2001.
[48] A.W. Sousa da Silva, W.F. Vranken, ACPYPE - AnteChamber PYthon parser interface, BMC. Res. Notes 5 (2012) 367, https://doi.org/10.1186/1756-0500-5-367.
[49] D. Van Der Spoel, E. Lindahl, B. Hess, et al., GROMACS: fast, flexible, and free, J. Comput. Chem. 26 (16) (2005) 1701–1718, https://doi.org/10.1002/jcc.20291.
[50] M.J. Abraham, T. Murtola, R. Schulz, et al., GROMACS: high performance molecular simulations through multi-level parallelism from laptops to supercomputers, SoftwareX 1–2 (2015) 19–25, https://doi.org/10.1016/j.softx.2015.06.001.
[51] T. Darden, D. York, L. Pedersen, Particle mesh ewald—an n.log(N) method for ewald sums in large systems, J. Chem. Phys. 98 (1993) 10089–10092, https://doi.org/10.1063/1.464397.
[52] B. Hess, H. Bekker, H.J.C. Berendsen, J.G.E.M. Fraaije, LINCS: a linear constraint solver for molecular simulations, J. Comput. Chem. 18 (1997) 1463–1472, https://doi.org/10.1002/(SICI)1096-987X(199709)18:12<1463::AID-JCC4>3.0.CO;2-H.
[53] G. Bussi, D. Donadio, M. Parrinello, Canonical sampling through velocity rescaling, J. Chem. Phys. 126 (2007) 014101, https://doi.org/10.1063/1.2408420.
[54] P.H. Hünenberger, Thermostat algorithms for molecular dynamics simulations, in: Dr.C. Holm, Prof.Dr.K. Kremer (Eds.), Advanced Computer Simulation. Advances in Polymer Science, Springer, Berlin, 2005, pp. 105–149.
[55] M. Parrinello, A. Rahman, Crystal structure and pair potentials: a molecular-dynamics study, Phys. Rev. Lett. 45 (1980) 1196–1199, https://doi.org/10.1103/PhysRevLett.45.1196.